Numerical Simulation of Superradiance in Rotating Black Holes

Mahtab C[1] and Mahtab Chowdhury[1]

[1]Affiliation not available

December 23, 2022

Numerical Simulation of Superradiance in Rotating Black Holes

Mahtab Chowdhury[1]*

Abstract
Due to the superradiance phenomenon, energy could be extracted from a rotating black hole (RBH) by an incident wave with certain initial conditions. The aim is to observe this process by numerical simulation.

Keywords
Superradiance — Black Holes — Waves

Author Contact: mahtab.chowdhury3211@gmail.com

Contents

Introduction

The first theoretical background of an energy-momentum extraction phenomenon to an RBH is proposed by Penrose [1], showing that a scattering process in the ergosphere can generate high-energy particles, escaping from the ergoregion at large distances from the RBH [2]. Later, Teukolsky and Press [3] studied a similar process, called superradiance, for its gravitational and electromagnetic analog. The motivation for studying this type of phenomena is to try to understand the formation of astrophysical jets (high energy and highly collimated matter flows) emerging from supermassive RBH. While until recently the general belief was that these were due to a magnetohydrodynamical phenomenon, a consequence of magnetic currents in the accretion disk (Blandford and Znajek, 1976), analyses of particle geodesics in a Kerr background gave hints that purely gravitational effects (in particular by the pair generation of the Penrose process) may be playing a more important role than previously thought. In numerical studies such as [4] it is observed through the Monte Carlo method that a large number of particles emerging from an RBH by the Penrose process would have a high degree of collimation. This type of result agrees with measurements in which a large percentage of the jet particles are found to have ultra-relativistic velocities [5], which is more in line with the model of a purely geometrical effect. In addition, the observation of charge-neutral particles forces a reconsideration of the magnetic effects of the magnetohydrodynamic model. In particular, in this work we studied the behavior of a scalar field (Klein Gordon). An important antecedent of the study of this type of fields in RBH can be seen in [6]; here, the superradiance phenomenon is observed. However, [7] repeated the study with another numerical method (purely spectral) and, unlike in [6], with an initial compact support data (equal to zero inside the ergoregion), and the incident wave, instead of extracting energy, is completely reflected at the edge of the ergoregion. The objective of this paper is to provide an analysis that helps to understand the difference between these two publications. The sections are arranged as follows. In Section 1 we present the problem and in Section 2 the different coordinates used in the code. In Section 3 we analyze how the flow we will study will be, Section 4 explains the initial data used and in Section 5 the wave equation it obeys. Section 6 has a description of how to read the images included, Section 7 the results obtained, in Section 8 the convergence is analyzed and finally in Section 9 the conclusions.

1. Problem

We want to analyze numerically the phenomenon of superradiance. Superradiance occurs when, under certain initial conditions, a wave heading towards an RBH returns later with more energy than it had at the beginning. This gain in wave energy is at the cost of extracting rotational energy from the RBH when it interacts with the ergoregion. To do the

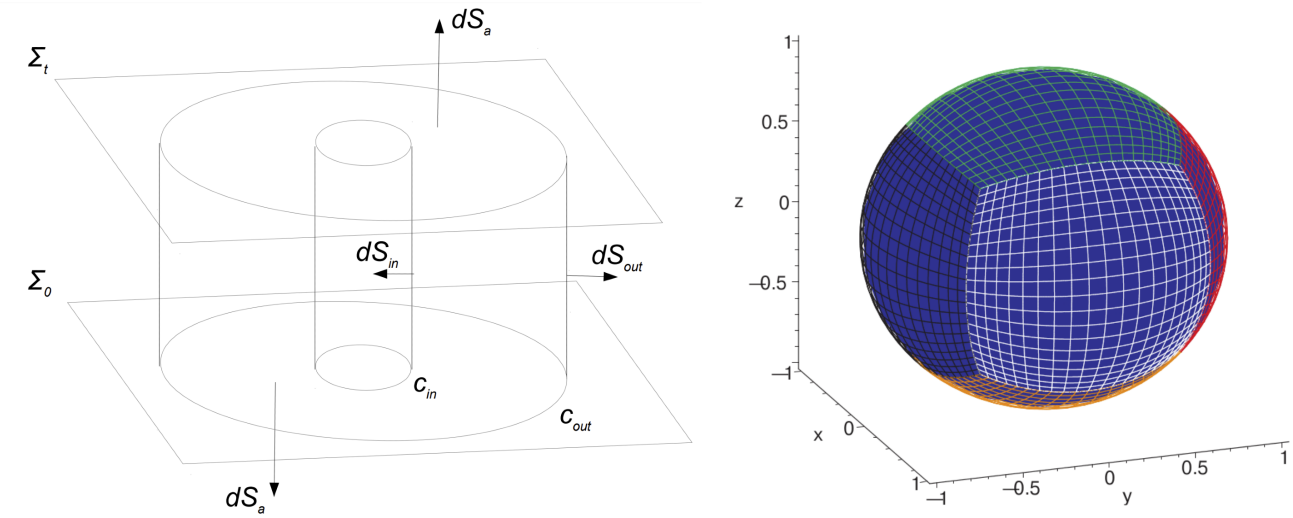

Figure 1. The left presents the field to be studied. The right shows the patches.

numerical study, we will then need to represent a region of space-time. First, we map the space-time with Cauchy surfaces, parameterized with a time t, and from each surface, we consider a section that encompasses the entire ergoregion and a portion of the surrounding spacetime. This region is shown in Figure 1. It represents two spatial Cauchy surfaces Σ_o and Σ_t, i.e. space at time. $t = 0$ and at a later time t, and on each of these surfaces we take two spheres: one of radius c_{in}, which is inside the outer event horizon (therefore also inside the ergoregion) and outside the inner event horizon; and another of radius c_{out}, outside the ergoregion. The succession of spheres on each surface between Σ_o and Σ_t will give us the two cylinders shown in the figure. Our total region of interest is the one that spans from the inner cylinder to the outer cylinder. It will be within this range that we will set the initial data. The data, which is initially far from c_{in}, will fall towards the RBH, will reach the ergoregion, and then, what did not fall within the RBH will leave the ergoregion heading now in the opposite direction towards c_{out}. Our way of analyzing if the superradiance phenomenon is occurring is by means of the flow. Suppose that the initial data is non-zero in the interval $[c_i, c_f]$ (with $c_{in} < c_i < c_f < c_{out}$), what we will do then is to take a radius c_{Flujo} between the initial data and the inner radius ($c_{in} < c_{Flujo} < c_i$) and calculate the flux passing through that sphere. If we wait long enough, all the data will pass through that region, reach the RBH, and pass back again on its return. Three situations can occur: that the total flux will be zero (as for example in Minkowski, whereas there is no black hole, all the wave returns in the same way); that the flux is greater than zero because part of the data was lost in the RBH (as will be the case in general for Kerr); or that it is negative. The latter would be the superradiant case since it would mean that it passed through c_{Flujo} with more energy on its return.

2. Coordinates

Since the numerical evolutions need a flat representation, each sphere is covered with six patches (see Figure 1), and a coordinate change is then performed, for each patch, from (t, x, y, z) to (t, a, b, c). The coordinate changes can be found in [8]. a and b are the coordinates that parameterize each patch for a fixed radius. That is, they represent the angular variables. While $c = \sqrt{x^2+y^2+z^2}$ is the Cartesian radius, and this is the coordinate in which the spheres discussed in Section 2 are represented. Since in this transformation, we work then with Cartesian radii, to be able to introduce the sphere c_{in} inside the event horizon r_+, it will be fundamental to see the form that have the horizons of the RBH, thought as ellipsoids in Cartesian coordinates (see Figure 2). But in addition, another complication arises: it is necessary that the propagation velocities in c_{in} are both directed towards the singularity (i.e., that the null velocities that form the cones are incoming), however in the event horizon the cone points outwards again because one of the propagation velocities changes sign again. Therefore c_{in} has to be contained between r_+ and r.

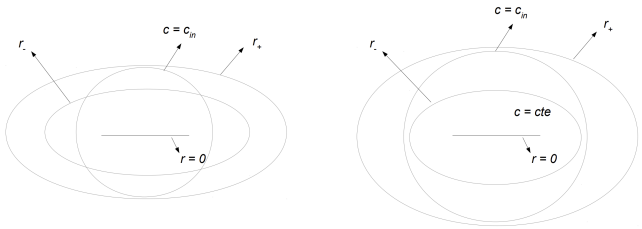

Figure 2. In-text Picture

The problem is that this is not always possible. If the angular velocity is very large, the ellipsoids flatten in such a way that it becomes impossible to place a sphere between them (as in the representation on the left in Figure 2). It was then necessary to find an angular momentum such that

a Cartesian sphere can be contained between the ellipsoids. Taking into account that the superradiance phenomenon is best observed for large annular velocities, the maximum possible value was sought, which was $a = \frac{J}{m} = 0.96$. To make sure that this sphere c_{in} is contained between the horizons, the sign of the wave propagation velocity at that radius is numerically controlled, making sure that both propagation directions have the same sign. Regarding the representation of the Kerr metric, the code uses Kerr-Schild coordinates:

$$ds^2 = -dt^2 + dx^2 + dy^2 + dz^2 + \frac{2Mr^3}{r^4 + a^2z^2}\left[\frac{r(x\,dx + y\,dy) - a(x\,dy - y\,dx)}{r^2 + a^2} + \frac{z\,dz}{r} + dt\right]^2$$

That is, it is of the form:

$$g_{ab} = \eta_{ab} + 2Hl_al_b$$

With $H = \frac{mr}{r^2 + a^2\cos^2\Theta}$ null with respect to η_{ab} and g_{ab}

This metric is then rewritten in terms of a lapse function and a vector shift [2]. For this we foliate with spatial Cauchy surfaces, Σ_t, parameterized by a global function of time t. If n^a is a unit vector normal to Σ_t (i.e. temporal), then we can obtain the metric of the spatial surface:

$$h_{ab} = n_an_b + g_{ab}$$

And we see that $h_{ab}n^a = 0$, that is h_{ab} is the spatial metric induced on the surface Σ_t. Now (with t^a such that $t^a\nabla_a t = 1$) we decompose t^a in the direction of n^a and Σ_t respectively (i.e. $t^a = an^a + \beta^a$):

$$\alpha = -t^an_a$$

$$\beta_a = h_{ab}t^b$$

The components of the metric and the relationship between the two coordinates can be found in Appendix A.

3. Flow

Let us now look at a way of calculating the flux that will help us to determine superradiance. The current j^a is given by:

$$j^\mu = -T^\mu{}_\nu k^\nu$$

With $T^\mu{}_\nu$ the one corresponding to that of a scalar field:

$$T_{\mu\nu} = \partial_\mu\Phi\partial_\nu\Phi - \frac{1}{2}g_{\mu\nu}(\partial\Phi)^2$$

and $k = \partial/\partial t$. Then

$$j^\mu = \partial^\mu\Phi\partial_t\Phi - \frac{1}{2}k^\mu(\partial\Phi)^2$$

Moreover, since the metric does not depend explicitly on time, k is Killing, and then this current is conserved $\nabla_a j^a = 0$. If we integrate in the region of interest presented in Figure 1, we can then apply Stokes on the volume studied and obtain:

$$0 = \int_S \nabla_a j^a\sqrt{-g}\,d^4x = \int_{\partial S} j^a dS_a$$

$$0 = \int_{border_{out}} j^a d\hat{S}_a - \int_{border_{in}} j^a d\hat{S}_a + \int_{\Sigma_t} j^a dS_a - \int_{\Sigma_o} j^a dS_a$$

The last two terms represent the total energy between the spheres (the lids of the hollow cylinder). The term integrated over Σ_0 corresponds to the initial energy, while the one integrated over Σ_t is the energy at time t (final energy). Let us analyze one of the first two terms, which correspond to the flow integrating in time over a sphere. We must integrate, first over the surface of a sphere, and then that sphere over time.

$$F = \int_{border} j^a d\hat{S}_a = \int_{t_i}^{t_f}\int_{sphere} j^a\frac{(dc)_a}{|dc|}dV$$

The volume element for that case will be:

$$dV = det(-M)da\,db\,dt$$

With M the metric induced tensor for a constant r. The minus comes from the fact that the induced on a surface $c = cte$ has signature $(-,+,+)$. If we contract (dc) with the current of (1), we obtain:

$$j^\mu\frac{(dt)_\mu}{|dc|} = \partial_t\Phi(g^{cj}\partial_j\Phi - g^{tc}\partial_t\Phi)\frac{1}{\sqrt{g^{cc}}}$$

That is, we are integrating the Poynting vector. For example we see that for Minkowski ($g^{tc} = 0$ and$g^{cc} = 1$) we are left with $\partial_t\Phi\partial_c\Phi$. For the energy terms, we have:

$$E = \int_\Sigma j^a dS_a = \int_{top} j^a\frac{(dt)_a}{|dt|}dV$$

$$j^\mu\frac{(dt)_\mu}{|dt|} = \frac{1}{2}(g^{tt}\partial_t\Phi\partial_t\Phi - g^{ij}\partial_i\Phi\partial_j\Phi)\frac{1}{\sqrt{-g^{tt}}}$$

4. Initial Data

We see for example in [9] that to observe superradiance, the scalar field must be of the form:

$$\Phi = \Phi_0\cos(\omega t - m\phi)$$

Where m is the quantum number corresponding to the angular momentum (the m of the Y_{lm}) and is the frequency which must be in the superradiant interval. Since the average power lost on the horizon is given by:

$$P = \frac{1}{2}\Phi_0^2 A\omega(\omega - m\Omega_H)$$

With $\Omega_H = \frac{a}{r^2+a^2}$, this power will be negative when $0 \leq \omega \leq m\Omega_H$. This is then the superradiant interval. In our case we will use as initial data a field of the form:

$$\Phi = f(r)\sin^2\theta\frac{cos(w(r - r_m) - m\phi)}{r}$$

Where here also r is the Cartesian radius, that is, c in (t,a,b,c), and $r_m = \frac{r_i+r_f}{2}$ is the center of the data, whose support is given by the function f:

$$f(r) = \frac{1}{N}(r-r_i)^n(r-r_f)^n$$

for $r \in [r_i, r_f]$ and $f(r) = 0$ for radii outside that interval. $N = (r_m - r_i)^n(r_m - r_f)^n$ is a normalization so that $f(r_m) = 1$. Being polynomial, this function gives it a pulse shape and becomes zero at its extremes, so that the initial data is smooth. For this wave to propagate towards the event horizon we must fix its time derivative. We will do this by deriving as if we had plane geometry, since all we are looking for is an initial condition for the velocity that directs most of the wave towards the RBH . With a sufficiently large r_i we can see that the wave is indeed directed towards the RBH. The condition for this to occur in plane geometry is:

$$\Phi = \frac{\partial\Phi}{\partial r} = n\left(\frac{f(r)}{(r-r_i)} + \frac{f(r)}{(r-r_f)}\right)\sin^2\theta\,\frac{\cos(\omega(r-r_m)-m\phi)}{r} - \omega f(r)\sin^2\theta\,\frac{\sin(\omega(r-r_m)-m\phi)}{r}$$

In the following section we will see the evolution of the initial data considering the Kerr geometry.

We must change the free parameters (n, r_i, r_f, ω, m) to maximize the proportion of the wave returning from the RBH. For this we started from the initial data used in [7], and from there we tested by making small variations to the parameters and controlling the flux integral. It is observed that the proportion of the wave that falls in the RBH is smaller for waves of large non-zero domain, but it was also noted that the distance between the end of the ergosphere and the beginning of the pulse must be large, therefore it was taken $r_i = 41$ and $r_f = 79$. The optimum power found is $n = 2$ and the spherical harmonic $l = 2$, with $m = 2, -2$ being the corresponding values for a wave co-rotating with the RBH and counter-rotating respectively. Finally ω will tell us, for a fixed ϕ, how many cycles enter the pulse. Since the extracted power is given by (2), it will be maximum when $\omega = \Omega_H$ (which can be seen by deriving (2) with respect to ω and equaling zero). The parameters n, r_i, r_f and ω were the ones that most needed to be tested, because they are not only related to each other (for example when changing the interval $[r_i, r_f]$, changes r_m and therefore the number of cycles that will give us ω), but also because they intervene in the accuracy with which the data is represented. This occurs on the one hand because of the length of the domain, due to the number of points used to represent the wave, as well as the power of the polynomial, because if this is small, the junction between $f(r) \neq 0$ and $f(r) \neq 0$ is less smooth, but if it is very large, it is noted that the convergence worsens (since the accuracy of the derivative operators depends on the power). These dependencies with accuracy led to the fact that in many cases certain results that seemed good with a certain number of points became worse than others as the number of points increased, and it was then necessary to run simulations with many points to determine which one was adequate.

5. Wave Equation

The code was previously constructed to evolve Maxwell's equations in Kerr geometry, therefore it is necessary to rewrite the wave equation of a scalar field in terms of the variables available in the code. It can be seen (Appendix A) that the wave equation:

$$\Box\Phi = \nabla_a\nabla^a\Phi = \frac{1}{\sqrt{-g}}\partial_\nu(\sqrt{-g}g^{\nu\gamma}\partial_\gamma) = 0$$

It is verified if we evolve:

$$\partial_t\Phi = \beta^i\partial_i\Phi - \frac{\alpha}{\sqrt{h}}\partial_i(\sqrt{h}B^i)$$

With B^i evolving as:

$$\partial_t B^i = -\frac{1}{\alpha}\beta^i(\partial_t\Phi) - \alpha g^{ij}\partial_j\Phi$$

Therefore giving $\partial_t\Phi$ as in Section 4 and obtaining B^i from Φ, we have the evolution of the wave equation.

6. About the Images

Before going to the results, let's see how to interpret the images. As we said, each sphere of constant Cartesian radius is represented by six patches, therefore the representation of a spherical harmonic $l = 2$ when we put the disassembled sphere in a plane, will look like in Figure 3.

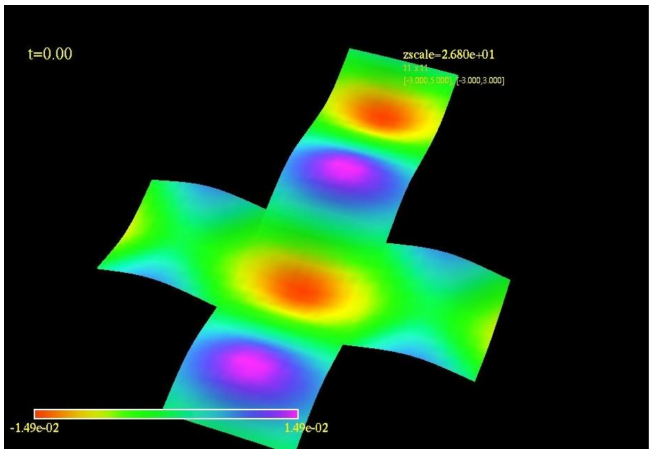

Figure 3. Constant Radius Cut

Then, if we now add the radial dimension, the result will be as shown in Figure 4.

However, in this last representation we cannot appreciate the value of the data at each point because we need an extra dimension, so the most practical way will be to make cross sections. For example, a possible cut would be to take from each sphere only its equator. Figure 5 shows how the cut was made and 6, its representation in the code.

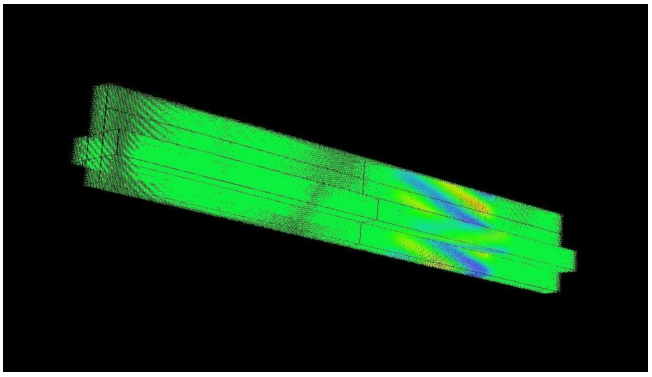

Figure 4. Complete Representation

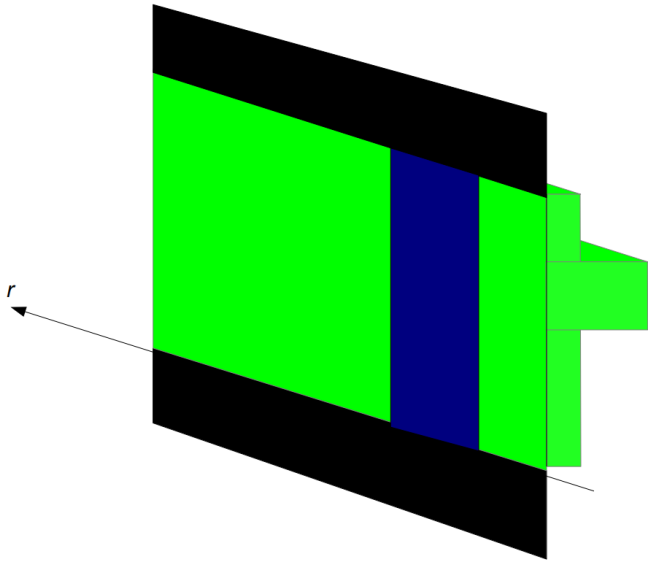

Figure 5. Cross Section

7. Results

The first thing to study is Minkowski because it is the simplest case and allows us to have a proof of the flow calculation, observing if the total flow for a fixed radius is zero. Given the singularity of coordinates at the origin, what was done was to simulate "a mirror" at a given radius. This means putting a boundary condition corresponding to the outgoing solution of the wave equation.

$$\dot{\Phi}_{mirror} = -\dot{\Phi}_{incident}$$

$$(\partial_r \Phi)_{mirror} = (\partial_r \Phi)_{incident}$$

And with that condition we control that the energy remains constant and that the total integrated flux is zero. In Figure 6 you can see the evolution of the wave and how it returns. On the right are the smallest radii (ending in c_{in}) and on the left are the large radii (ending in c_{out}). We see that the wave goes towards $r = 0$, reflects at a radius $r = 1.250$ and returns preserving the shape. Then in Figure 8 we can see that the energy remains constant, with a small perturbation on the order of one part in ten thousand at the time of reflection.

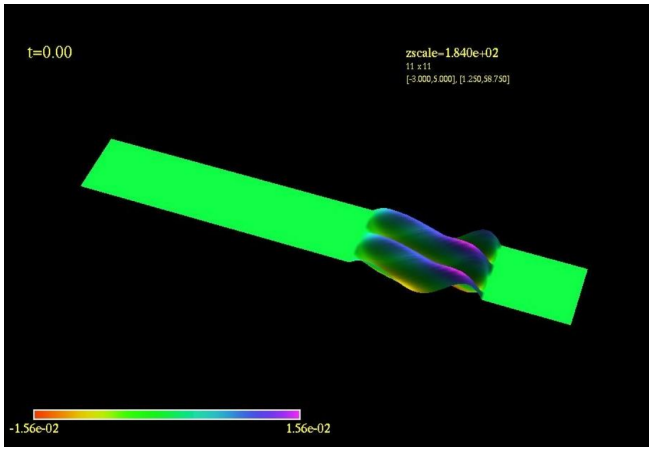

Figure 6. Cross Section

In Figure 9 we see that the integrated flux at $r = 3$ reaches a maximum when the whole wave passes, and then returns to zero when it returns. In addition, Figure 10 shows in detail the moment when the wave finishes returning, there you can see that it returns to zero with an error of less than one part in ten thousand.

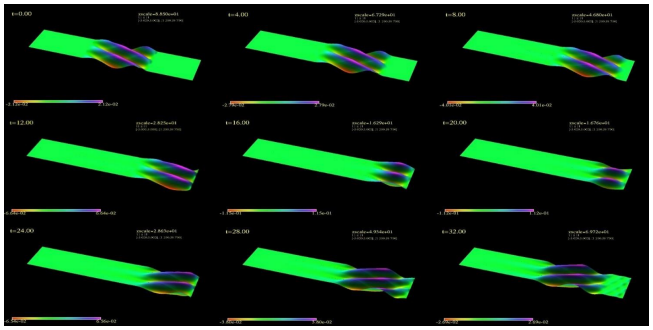

Figure 7. Evolution

In addition to testing the energy and flux, there is a third test that we can perform, which consists of relating both quantities. What was done is to calculate the energy in the region that occupies the initial data at time $t = 0$ and the flux in the lower limit of that same region. Then, as time passes, the wave will be leaving, and therefore decreasing the energy in that region, while the integrated flux will be increasing by the same amount. Therefore, adding both quantities we will have a test that combines them. This is shown in Figure 11. The reason why it falls at first is that here we are comparing two numerically distinct integrals: the energy is a spatial integral and therefore depends on the spatial steps, while the flux involves the combination of two spatial coordinates with a temporal one. So, for each time, we are taking an approximation of the flux integral, however we can see that when all the energy has left the region, the total value of the flux is equal to that of the energy in one part in ten thousand.

Let us now look at the Kerr case. The evolution, for the data presented in Section 4, is shown in Figure 12. We see that

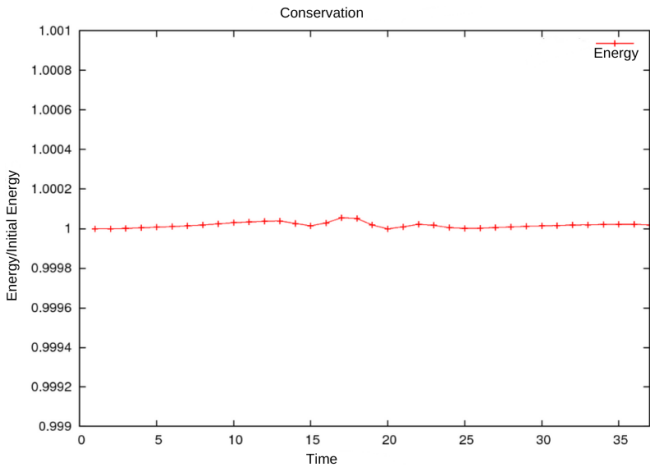

Figure 8. Energy

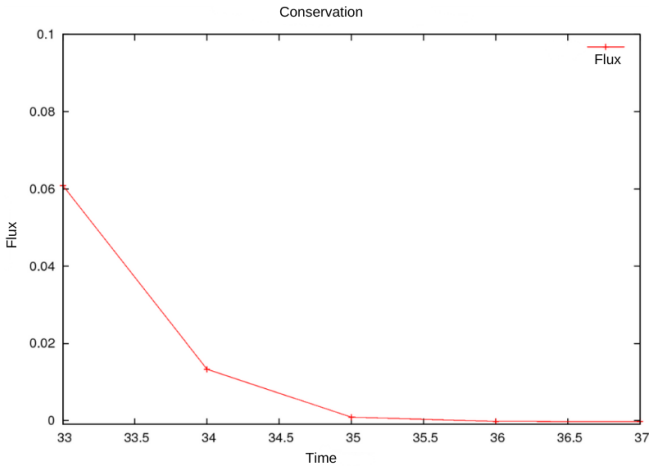

Figure 10

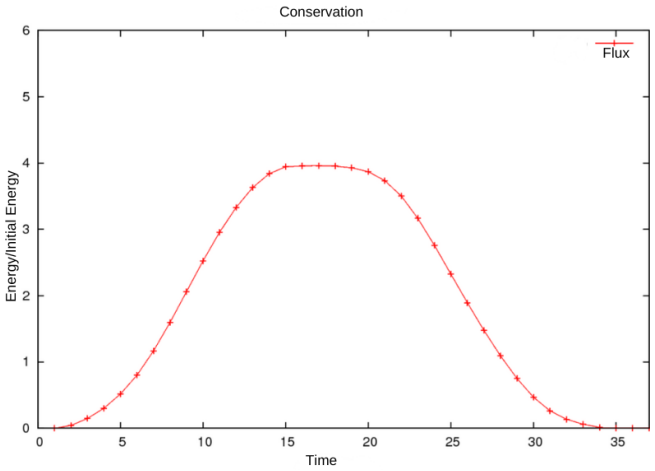

Figure 9. Flux

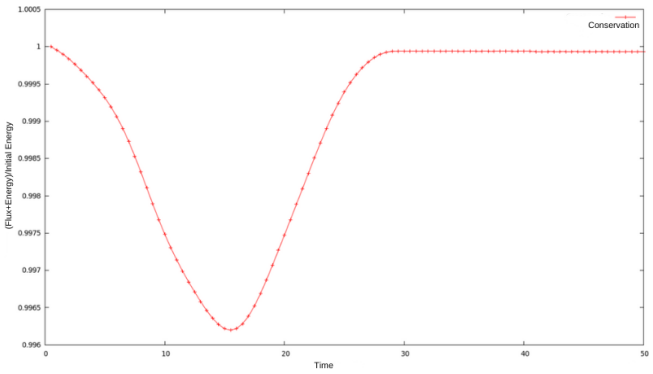

Figure 11. Conservation

the wave returns from the ergoregion maintaining the shape. The flow curve is presented in Figure 13 and the energy in Figure 14. Here the control of energy and flux was performed as in the Minkowski conservation. That is, we take an interval that covers only the initial data and we control how these variables evolve, first separately, and then their combination.

We see that the energy returns to its initial value, and that the total integrated flux is zero, i.e., we obtain the same result as for Minkowski: the whole wave returns. Figure 15 shows the relationship between the two quantities. The disturbance in the graph at the beginning is, as before, the consequence of the flux integral also being a time approximation

8. Convergence

In order to analyze the convergence of the code, the accuracy coefficient given by

$$Q(t) := \frac{u^{(1)}(t,x;\Delta t,\Delta x) - u^{(2)}(t,x;\Delta t',\frac{\Delta x}{2})}{u^{(2)}(t,x;\Delta t',\frac{\Delta x}{2}) - u^{(3)}(t,x;\Delta t'',\frac{\Delta x}{4})} = 2^q$$

Where Δx represents the spatial step (i.e. the total length divided by the number of grids) and the different Δt are taken in such a way that the quotient $\frac{\Delta t}{\Delta x} = 0.1$. The value of q will give us the order of the method used since we are comparing how the error changes as we double the number of points. In our case the grids used were (in the coordinates (a,b,c) presented in Section 1): $11x11x231$, $21x21x461$ and $41x41x921$. And with those points the result was the one presented in Figure 16.

The expected result was $q = 4$ because we are using a Runge-Kutta of order 4, however we see that we are converging to $q = 3$. This is probably because the number of points used is too few to obtain the optimal result. As the increase in the total number of points, the next step $(81x81x1841)$ exceeds the available resources in the cluster used, however we will try to perform this simulation in a larger cluster. As discussed in Section 5, it is also observed that for initial polynomial data of smaller powers the convergence has a lower order (perhaps due to the junction between the data support and the zero data), however for higher powers, where the junction is smoother, the data is concentrated in the center (it becomes sharper) and this also causes a decrease in the pressure. It should also be noted that although the polynomial form is the simplest way to represent the pulse, it is possible

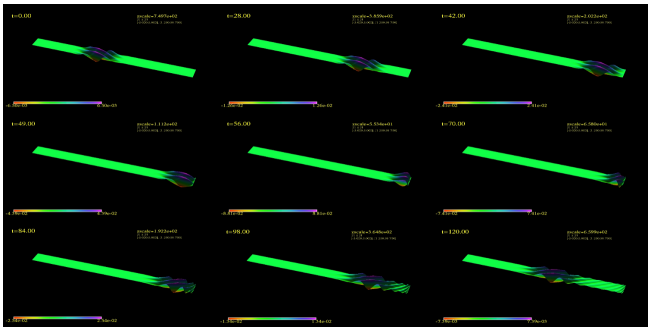

Figure 12. Evolution

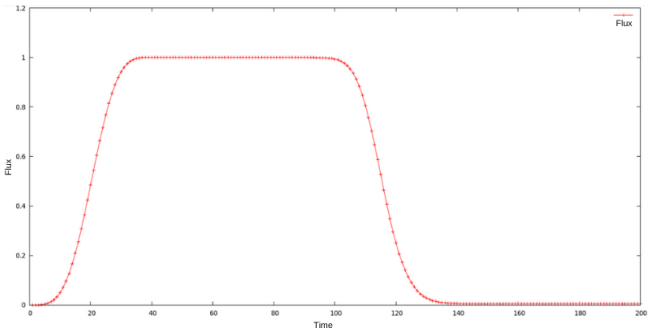

Figure 13. Flux

by means of Hermite polynomial interpolation to generate a data having a larger number of continuous derivatives.

9. Conclusions

The most important thing to note is that the result is similar to that obtained in [7], in which the incident wave is completely reflected. That is to say, the superradiance phenomenon was not found either. However, one of the main differences is that even for the cases of total reflection obtained, the interaction between the wave and the ergoregion is still considerable (i.e., the wave penetrates up to the ergoregion, while in [7] they observe that for the case of total reflection the wave does not enter the ergoregion). Since the way the wave extracts energy from the RBH is precisely through its ergoregion, the results lead to think that it is still possible to find a way to adjust the data in such a way that the phenomenon is observed. Another consideration is that the difficulties in placing a sphere of constant Cartesian radius between the horizons (as presented in Section 2), led to the maximum possible angular velocity being less than that used in [7] ($a = 0.96$ instead of $a = 0.99$). And since the superradiance phenomenon intensifies for larger angular momenta, the angular velocity may not have been sufficient. The next step is to extend what has been done for the case of electromagnetic waves to discover whether this total reflection phenomenon is in fact a feature of the scalar field. The code has incorporated the evolution of Maxwell's equations in Kerr (in fact, as shown in Section 6, they were used to form the scalar field by putting $E = 0$ and taking advantage of the evolution of B and its zero divergence) so

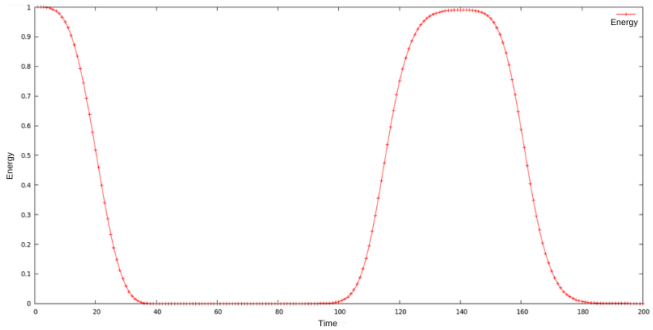

Figure 14. Energy

it is only necessary to put a suitable initial data to search for superradiance.

10. Appendix A

The metric components in terms of lapse and shift are:

$$g_{ab}((\partial t)^a,(\partial t)^b) = g_{00} = \beta^2 - \alpha^2$$

$$g_{ab}((\partial t)^a,(\partial x_i)^b) = g_{0i} = \beta_i$$

$$g((\partial x_i)^a,(\partial x_j)^b) = h_{ij}$$

While we can obtain components of the inverse by developing t^a:

$$g^{ab} = h^{ab} - n^a n^b$$

$$g^{ab} = h^{ab} - \frac{1}{\alpha^2}((\partial t)^a - \beta^a)((\partial t)^b - \beta^b)$$

$$g^{ab} = -\frac{1}{\alpha^2}(\partial t)^a(\partial t)^b + \frac{2}{\alpha^2}(\partial t)^a\beta^b + (h^{ab} - \frac{\beta^a\beta^b}{\alpha^2})$$

$$g^{00} = -\frac{1}{\alpha^2} \qquad g^{0i} = \frac{\beta^i}{\alpha^2} \qquad g^{ij} = h^{ij} - \frac{\beta^i\beta^j}{\alpha^2}$$

The correspondence between coordinates is:

$$H = \frac{1}{2}(-1 + \frac{1}{\alpha})$$

$$l^i = (\frac{1+2H}{2H})\beta^i$$

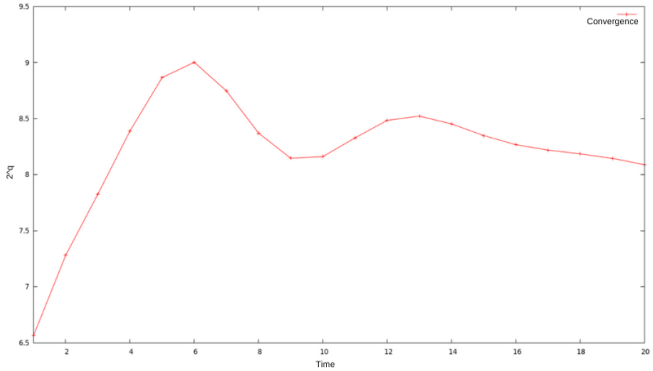

Figure 15. Convergence

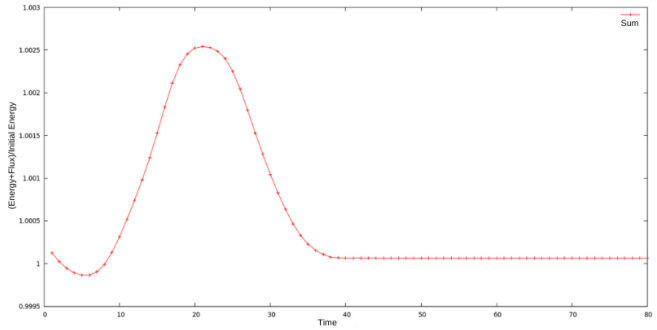

Figure 16. Conservation

11. Appendix B

To write the wave equation in terms of the fields in the code we start from:

$$\Box\Phi = \nabla_a\nabla^a\Phi = \frac{1}{\sqrt{g}}\partial_\nu(\sqrt{-g}g^{\nu\gamma}\partial_\gamma\Phi) = 0$$

Developing this term and noting that $\sqrt{-g} = \alpha\sqrt{h}$, we have

$$\Box\Phi = g^{00}\partial_{tt}\Phi + g^{0i}\partial_i\partial_t\Phi + \frac{1}{\alpha\sqrt{h}}\partial_i(\alpha\sqrt{h}g^{i0}\partial_t\Phi) + \frac{1}{\alpha\sqrt{h}}\partial_i(\alpha\sqrt{h}g^{ij}\partial_j\Phi) = 0$$

And now we replace by the components obtained in Section 2:

$$\partial_{tt}\Phi = \alpha^2 g^{0i}\partial_i\partial_t\Phi + \frac{\alpha}{\sqrt{h}}\partial_i(\alpha\sqrt{h}g^{i0}\partial_t\Phi) + \frac{a}{\sqrt{h}}\partial_i(\alpha\sqrt{h}g^{ij}\partial_j\Phi)$$

$$\partial_{tt}\Phi = \beta^i\partial_i\partial_t\Phi + \frac{\alpha}{\sqrt{h}}\partial_i(\frac{1}{\alpha}\sqrt{h}\beta^i\partial_t\Phi + \alpha\sqrt{h}g^{ij}\partial_j\Phi) \qquad (4)$$

And to write it using the magnetic field consider the expression of B^i:

$$\partial_t B^i = -\frac{1}{\alpha}\beta^i(\partial_t\Phi) - \alpha g^{ij}\partial_j\Phi \qquad (5)$$

If we now multiply (5) by $\sqrt{h}$ and then derive:

$$\partial_i(\sqrt{h}\partial_t B^i) = -\partial_i(\frac{1}{\alpha}\sqrt{h}\beta^i\partial_t\Phi + \alpha\sqrt{h}g^{ij}\partial_j\Phi)$$

Replacing in (4):

$$\partial_{tt}\Phi = \beta^i\partial_i\partial_t\Phi - \frac{\alpha}{\sqrt{h}}\partial_i(\sqrt{h}\partial_t B^i)$$

Therefore we evolve $\partial_t\Phi$ as:

$$\partial_t\Phi = \beta^i\partial_i\Phi - \frac{\alpha}{\sqrt{h}}\partial_i(\sqrt{h}B^i)$$

References

[1] PENROSE, R., FLOYD, R. M. (1971). Extraction of rotational energy from a black hole. Nature Physical Science, 229(6), 177–179. https://doi.org/10.1038/physci229177a0

[2] Wald, R. M. (1984). General relativity. General Relativity. https://doi.org/10.7208/chicago/9780226870373.001.0001

[3] Teukolsky, S. A., Press, W. H. (1974). Perturbations of a rotating black hole. III - interaction of the hole with gravitational and electromagnetic radiation. The Astrophysical Journal, 193. https://doi.org/10.1086/153180

[4] Williams, R. K. (2004). Collimated escaping vortical polaree+jets intrinsically produced by rotating black holes and Penrose Processes. The Astrophysical Journal, 611(2). https://doi.org/10.1086/422304

[5] Junor, W., Biretta, J. A., amp; Livio, M. (1999). Formation of the radio jet in M87 at 100 Schwarzschild radii from the central black hole. Nature, 401(6756). https://doi.org/10.1038/44780

[6] Andersson, N., amp; Papadopoulos, P. (1998). Dynamics of scalar fields in the background of rotating black holes. II. A note on Superradiance. Physical Review D, 58(8). https://doi.org/10.1103/physrevd.58.087503

[7] Csizmadia, P., László, A., amp; Rácz, I. (2012). On the use of multipole expansion in time evolution of nonlinear dynamical systems and some surprises related to superradiance. Classical and Quantum Gravity, 30(1). https://doi.org/10.1088/0264-9381/30/1/015010

[8] Lehner, L., Reula, O., amp; Tiglio, M. (2005). Multi-block simulations in general relativity: High-order discretizations, numerical stability and applications. Classical and Quantum Gravity, 22(24). https://doi.org/10.1088/0264-9381/22/24/006

[9] Townsend, P. K. (1997, July 4). Black holes. arXiv.org. Retrieved from https://arxiv.org/abs/gr-qc/9707012